Chinese Chemical Letters 37 (2026) 111958

Contents lists available at ScienceDirect

Chinese Chemical Letters

journal homepage: www.elsevier.com/locate/cclet

Mediating electron delocalization of surface palladium atoms by diethylamine ligand for efficient CO_2 electroreduction

Mulin Yu[a], Shuo Liu[a], Yufeng Tang[a], Guoqiang Lu[a], Linbo Liu[a], Pengfei Sui[b], Xianzhu Fu[c], Subiao Liu[a,*], Yifei Sun[d], Jingli Luo[b,c]

[a] School of Minerals Processing and Bioengineering, Central South University, Changsha 410083, China
[b] Department of Chemical and Materials Engineering, University of Alberta, Edmonton, Alberta T6G 1H9, Canada
[c] College of Materials Science and Engineering, Shenzhen University, Shenzhen 518060, China
[d] College of Energy, Xiamen University, Xiamen 361005, China

ARTICLE INFO

Article history:
Received 11 June 2025
Revised 11 October 2025
Accepted 13 October 2025
Available online 14 October 2025

Keywords:
Electrochemical CO_2 reduction reaction
Ligand effect
Hydrogen bond
Pd electrocatalyst
Electron delocalization

ABSTRACT

Functionalizing ligands on surface metal atoms has been implemented to tune the adsorption behaviors of intermediates in electrochemical CO_2 reduction reaction (CO_2RR). However, it is always bound within an unfavorable linear scaling relationship of the synchronously changed adsorption energies of intermediates. To break it, a win-win diethylamine (DEA)-mediated strategy was proposed to functionalize surface Pd atoms by exchanging the residual oleylamine (OAm) on ultrafine Pd nanoparticles (Pd NPs) with DEA. The molecular dynamics simulations, coupled with *in situ* Fourier transform infrared spectroscopy results, revealed that DEA hindered less toward CO_2 than H_2O on Pd NPs surface, and induced more CO linear configuration intermediate ($^*CO_L$), indicative of ease CO_2 transport and CO desorption. Additionally, computational calculations implied that -NH- in DEA delocalized more electrons to surface Pd atoms and formed H-bond with *COOH, asynchronously changing the adsorption energies of *COOH and *CO, which enabled a CO Faraday efficiency (FE_{CO}) close to 100% in an ultrawide potential window and a stability of over 50 h with a FE_{CO} over 90%. This study dexterously addresses the residual issue of end-blocking agents on metal nanostructures from synthesis, and synchronously realizes the surface molecular functionalization, paving a smart avenue to design high-performance electrocatalysts.

© 2025 Published by Elsevier B.V. on behalf of Chinese Chemical Society and Institute of Materia Medica, Chinese Academy of Medical Sciences.

The sharply growing CO_2 concentration in the atmosphere has drawn particular attention worldwide due to the severe climate issues caused by the global warming, which makes an appeal for reducing CO_2 emission from the source, and ultimately reaching the carbon-neutral synthesis from CO_2. When powered with intermittent renewable energy sources, electrochemical CO_2 reduction reaction (CO_2RR) to produce C_1 products (*e.g.*, CO and HCOOH) stands out from various CO_2 conversion routes [1–3], especially on palladium (Pd)-based electrocatalysts. Different from other noble metals (*e.g.*, Au, Ag, Pt, Ru), Pd nanostructures normally display a comparable current density (j) at a desirable overpotential (η), and a tunable selectivity toward CO or HCOOH formation [4,5]. However, the unavoidable CO poisoning caused by the high adsorption energy CO on Pd(111) surface would result in the accumulation of *CO and hindrance of further C–O bond breakage [6,7]. Moreover, the difficult CO desorption hinders CO_2 adsorption on the surface because of the lack of adsorption sites, and the prolonged CO coverage induces surface reconstruction and changes in electronic configuration of Pd-based electrocatalysts, ultimately leading to electrocatalyst deactivation and stability decay [8,9]. In addition, due to the severe agglomeration of Pd nanoparticles (Pd NPs) during long-term operation, and the formation of PdO_x caused by the reaction between the oxygen species in the electrolyte and the surface Pd atoms [10,11]. Pd-based electrocatalysts are also prone to deactivation and structure reconstruction during CO_2RR, which, as a result, lead to a poor stability. To this end, various design strategies, *e.g.*, crystal facet control [12,13], assembling heterostructures [14], alloys [15], metal-based compound nanohybrids [16], surface modification [5], a different anoded-coupled reaction systems [17–19] have been proposed to improve CO_2RR performance. However, a concomitant issue inevitably occurs that the long-chain alkyl compounds/polymers (*e.g.*, polyvinylpyrrolidone (PVP), oleylamine (OAm) and cetyltrimethyl ammonium bromide (CTAB)) only act as an end-blocking agent for the synthesis of colloids or nanoparticles with a controllable size and/or shape, which are difficult to be completely removed, and sometimes even block the exposure of

* Corresponding author.
E-mail address: subiao@csu.edu.cn (S. Liu).

https://doi.org/10.1016/j.cclet.2025.111958
1001-8417/© 2025 Published by Elsevier B.V. on behalf of Chinese Chemical Society and Institute of Materia Medica, Chinese Academy of Medical Sciences.

electroactive sites on material surface. Upon acting in contravention, retaining the residue on the surface or exchanging it with certain ligands holds the potential to tune the physiochemical properties of material surface at molecular level, thereby affecting the electronic states and the freedom degrees of active centers, which ultimately regulate the reaction pathways for various target products toward CO_2RR [20,21].

In fact, a consensus on the ligand effect has been reached that the surface ligands tune the CO_2RR performance mainly from two angles, *i.e.*, the steric effect caused by different branch chain number, chain length and molecule spacing, and the electronic effect induced by various electron-donating and electron-withdrawing groups. To be specific, the ligands can not only spatially restrict a particular conformation of adsorbed intermediates and/or prevent reactants from contacting the material surface, but also modulate the electron density *via* the Lewis acid-base interaction to tune the material electronic structure. Previous studies have reported using macromolecule or long-chain organic ligands to promote the interplay between intermediates and metal active sites by constructing rigid organic-modified layers with an intermolecular van der Waals interaction. However, the severe coverage of ligands on metal surface blocks CO_2 accessibility to active sites. In the meantime, due to the lack of strong intermolecular interactions between various small organic ligands, building rigid channels on metal surface only partially but insufficiently regulates H_2O and dissolved CO_2 diffusions, and intermediate adsorption and/or desorption behaviors toward efficient CO_2RR.

In recent years, amine-functionalized metal-organic frameworks (MOFs) and molecular complexes have demonstrated considerable potential in CO_2RR through various methods (*e.g.*, tailoring central metal node [22], changing functional group [22,23], adjusting local electronic distribution [24] and forming hydrogen bonding networks [25]) to control the adsorption behaviors of intermediates. Inspired by these molecular-level design principles, our work extends the concept to nanostructured catalysts by grafting alkylamine ligands onto the surface of Pd NPs. Notably, amino [26], pyridinyl [27], and imidazole [28] could selectively construct metal-ligand interfaces, which further interact with reactants and/or intermediates with the aid of C–N bonds and/or H-bonds. Moreover, due to the electronegativity difference between the central heteroatoms in the ligand and the adjacent atoms in the surface metal, the electronic distribution on metal surface would be rearranged, thus leading to the shift in the d-band center of surface metal. Inspired by this, the diethylamine (DEA), as a small amine molecule, has been inferred effective to promote CO_2RR by strongly adsorbing on the metal surface through forming covalent bonds and/or coordinated covalent bonds with surface metal atoms induced by the lone pair electron of its N atom. More importantly, DEA, also acting as an intermediate ligand, is widely employed to exchange or replace other macromolecular long chain cap ligands (*e.g.*, PVP, OAm, and CTAB) that are difficult to be removed from metal surface [29]. It is worth noting that the difference in spatial configuration between DEA and OAm could change the adsorption configurations of CO_2 and its intermediates on surface Pd atoms. Moreover, the long alkyl chain of OAm limits its electron donation ability, whereas DEA with two short branched-chains is easier to transfer more electrons to surface Pd atoms, thus weakening the adsorption of *CO and improving the selectivity of CO [30,31]. Thus, the "one stone killing two birds" postulation addresses the residual issue of end-blocking agents on metal surface for specific nanostructure synthesis in organic media, and synchronously introduces the surface molecular functionalization, *i.e.*, ligand effect, to induce electron redistribution on N-mediated surface metal atoms and their associated electronic structure tuning for efficient CO_2RR.

To validate it, DEA was assembled on the surface of ultrasmall Pd NPs (DEA-Pd NPs) by exchanging the residue OAm ligands on Pd NPs (OAm-Pd NPs). The DEA-Pd NPs achieved a CO selectivity of close to 100% in a wide potential window of $-1.3 \sim -0.7$ V. The density functional theory (DFT) calculations revealed that the donating effect of N in DEA delocalized the electrons on the surface Pd atoms to the lower energy orbital, resulting in a negative shift of the d-band center, which weakened the adsorption of *COOH and *CO intermediates. Moreover, the H-bond formed between the N-H in DEA and the *COOH increased the adsorption energy of *COOH. This targets in tuning the binding energies of various intermediates during CO_2RR, which fundamentally addresses the issues of difficult *COOH adsorption and *CO desorption, and breaks the unfavorable linear scaling relationship of their simultaneous increase or decrease.

The introduced ligands on surface metal atoms inevitably influence the gas-liquid (CO_2–H_2O) balance adjacent to the active site [32], which regulates the associated CO_2 mass transfer and the final CO_2RR kinetics. To explore the effects of DEA on CO_2 and H_2O diffusion behaviors, MD simulations were first conducted to obtain the time sequence of typical snapshots of H_2O and CO_2 diffusion (Figs. S1a–c in Supporting information). Clearly, different from the random transportation behaviors on Bare-Pd NPs surface, H_2O and CO_2 diffusions were gradually limited when DEA was uniformly grafted on Pd NPs, and were completed prevented at 400 ps (Fig. 1a–c). This was further quantitatively determined by the diffusion coefficient (DC), as judged from the slope in Fig. 1d. The DC(CO_2) of DEA-Pd NPs (0.272×10^{-2} Å^2/ps) was smaller than that of Bare-Pd NPs (9.475×10^{-2} Å^2/ps), while the DC(H_2O) of Bare-Pd NPs (0.163×10^{-2} Å^2/ps) was larger than that of DEA-Pd NPs (0.143×10^{-2} Å^2/ps). This indicated that DEA limited both CO_2 and H_2O diffusions on Pd NPs surface, with a larger impact on CO_2 due to the larger diameter ($d = 3.3$ Å) of CO_2 than that ($d = 2.8$ Å) of H_2O. Notably, although CO_2 exhibited a stronger hindrance effect for diffusion on the surface of DEA-Pd NPs due to the larger molecule size than H_2O, it was not the sole determinant for diffusion behavior. Based on this, the radial distribution functions (RDFs) of CO_2 and H_2O were obtained to further reflect the density of CO_2 and H_2O near Pd NPs surface, *i.e.*, the accessibility to Pd NPs surface. Apparently, the density of CO_2 on Bare-Pd NPs and DEA-Pd NPs, reflected by g(r) values in Fig. 1e, were higher than that of H_2O. Nevertheless, the g(r) values of CO_2 and H_2O on DEA-Pd NPs were lower than those on Bare-Pd NPs, indicating that DEA reduced the probability of CO_2 and H_2O reaching the surface of Pd NPs.

By comparing the reduction degree of Pd-O (CO_2) and Pd-O (H_2O) (*i.e.*, the value of Δg(r)), it was found that Δg(r)CO_2 was significantly smaller than Δg(r)H_2O, proving that the hindrance degree of DEA toward CO_2 to Pd NPs surface was smaller than that toward H_2O. It is also worth noting that the V-shaped H_2O structure holds the potential to form strong H-bonds, making it more susceptible to be trapped by DEA within the H-bond network, leading to a slower diffusion [33,34]. In contrast, the nonpolar CO_2 molecule does not engage in H-bonding with DEA, which causes a less diffusion hindrance tread in reality, and an easier CO_2 diffusion to the DEA-Pd NP surface. Moreover, the –NH– and $-C_2H_5$ groups in DEA could induce a stable adsorption layer on the Pd surface and create a hydrophobic microenvironment [35,36], which reduced the affinity of Pd NPs for polar molecules, thus limiting the diffusion of H_2O molecules. In addition, the diffusion of H_2O molecule on DEA-Pd NPs was restricted by the solvation effect, since the polar H_2O molecule could form H-bonds with surrounding H_2O molecules or other polar molecules, and the H-bond network traps H_2O molecule, and restricts its diffusion. In contrast, nonpolar CO_2 exhibits a weaker solvation effect, and diffuses more

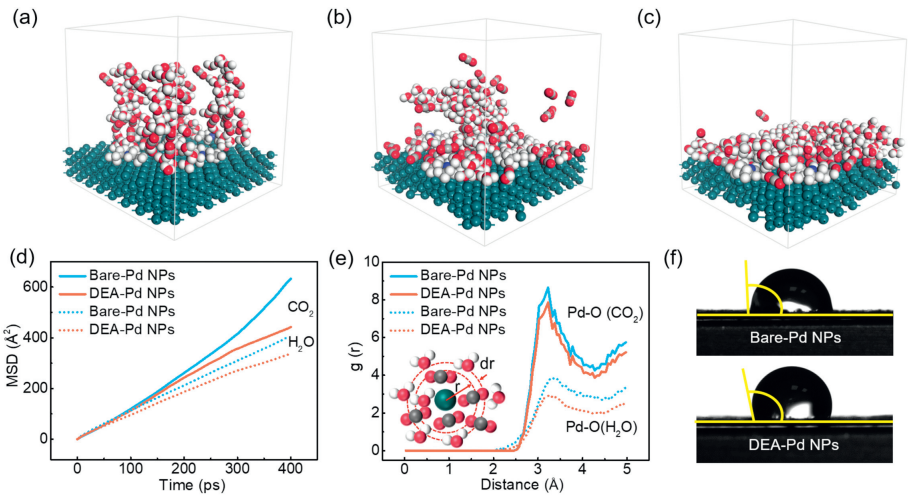


Fig. 1. Typical snapshots of H_2O and CO_2 diffusion on DEA-Pd NPs at (a) 0 ps, (b) 200 ps and (c) 400 ps. (d) Fitted MSD *versus* time for H_2O and CO_2 diffusion. (e) RDFs of H_2O and CO_2. (f) Contact angles of Bare-Pd NPs and DEA-Pd NPs.

freely in solution [37,38]. It was further verified by the larger contact angle of 106.1° on DEA-Pd NPs relative to that of 89.9° on Bare-Pd NPs (Fig. 1f, Figs. S2 and S3 in Supporting information). Notably, CO_2 primarily diffused in its dissolved form (HCO_3^- or CO_2 hydrate) on a hydrophilic surface, since the hydrophilic surface tended to form a thick water layer, which prolonged the diffusion pathway of the dissolved CO_2 and slowed its mass transfer rate. However, it could diffuse in the form of gas molecules on a hydrophobic surface, because the hydrophobic surface could reduce the thickness of water layer, allowing gaseous CO_2 to approach to the catalyst surface more easily, and consequently improving its diffusion efficiency [39–41]. In addition, instead of rapidly diffusing away from the surface, the DEA-functionalized Pd surface prolonged the residence time of CO_2 on Pd atoms since the "molecular network" formed by DEA can effectively confine CO_2 within it, thereby accelerating the subsequent CO_2RR.

DEA-Pd NPs were synthesized by a ligand exchange method [29], as schemed in Fig. 2a. Specifically, palladium(II) acetylacetonate was reduced to Pd NPs in OAm solution, followed by the addition of an appropriate amount of DEA solution dispersed in isopropyl alcohol to exchange the residue OAm on Pd NPs. Notably, DEA was a branched amine with stronger Lewis's basicity, and the lone pair electrons of its N atom can more effectively coordinate with the empty orbitals of Pd, forming a more stable Pd–N bond, thereby enabling the original end-capping ligands OAm to be effectively exchanged and removed. The transmission electron microscopy (TEM) image (Fig. 2b and Fig. S4 in Supporting information) confirmed that DEA-Pd NPs, OAm-Pd NPs and Bare-Pd NPs displayed a highly monodispersed spherical morphology on carbon black, with an average size of 5.16 ± 0.46 nm (Fig. 2c and Fig. S5 in Supporting information), revealing that the ligand introduction had no impact on the size of Pd NPs, thus eliminating the size effect interference on CO_2RR performance. The high-resolution TEM (HRTEM) image (Fig. 2d) and X-ray diffraction (XRD) pattern (Fig. S6 in Supporting information) confirmed the crystallinity nature of DEA-Pd NPs, and the lattice fringe spacing of 0.224 nm well corresponded to the face-centered cubic Pd(111) (JCPDS No. 01-1201). Besides, the energy-dispersive X-ray (EDX) elemental mappings presented a uniform distribution of the characteristic N element in DEA (Fig. 2e) and OAm (Fig. S7 in Supporting information) on Pd NPs. To further confirm the existing form of N in DEA with surface Pd atoms, FTIR was employed, as shown in Fig. 2f and Fig. S8 (Supporting information). Clearly, the as-synthesized OAm-Pd NPs before ligand exchange showed prominent vibrational peaks at 2923 and 2842 cm^{-1}, corresponding to the symmetric stretching C–H and asymmetric C-H of OAm, respectively. After ligand exchanging with DEA, the two vibrational peak intensities of DEA-Pd NPs were weakened, and well-resolved peaks belonging to –NH– group at 668 cm^{-1} were remarkedly strengthened, implying the successful ligand exchange of long-chain OAm by DEA [42,43].

X-ray photoelectron spectroscopy (XPS) was then performed (Fig. S9 in Supporting information), and the presence of Pd^{2+} peak in the XPS spectrum of Pd 3d (Fig. 2g and Fig. S10 in Supporting information) was attributed to the partial surface oxidation after exposure to air, leading to the formation of PdO or $Pd(OH)_2$ species on the surface [44,45]. Notably, the Pd 3d spectrum was negatively shifted by about 0.30 eV on DEA-Pd NPs as compared to that on Bare-Pd NPs. This is because the strong Pd–N interaction caused more electrons to be transferred from the amino ligand to the surface Pd atom, thus increasing the electron density of the surface Pd atoms [46–49]. Notably, a slight negative shift (~0.15 eV) in the Pd 3d binding energy was observed after ligand exchange, confirming an increased electron density on Pd from stronger electron donation by DEA. Again, the unique N 1s signal of DEA-Pd NPs and OAm-Pd NPs were observed in Fig. 2h and Fig. S11 (Supporting information), and the peak of the –NH– typically appeared in the binding energy range of the N 1s orbital, but its exact position was mainly depended on the chemical environment. Apparently, the peak at 400.4 eV in N 1s was attributed to the Pd-N bond, while the peak at 398.4 eV corresponded to the C–N bond [50–52], verifying that –NH– in DEA formed covalent bonds with surface Pd atoms. It is worth noting that the area of C–N bond in OAm-Pd NPs was significantly larger than that of Pd–N bond, while the opposite was true for DEA-Pd NPs, which indicated that DEA had successfully exchanged OAm. In addition, we further analyzed the C 1s spectrum (Fig. S12 in Supporting information). It was found that the proportion of C–C bond in OAm-Pd NPs (60.52 %) was higher than that in DEA-Pd NPs (44.48 %), while the proportion of C–N bond was higher in DEA-Pd NPs, since the long chain OAm possessed more C atoms. Obviously, the abovementioned results indicated that a large amount of OAm has been successfully exchanged by DEA.

CO_2RR activities on DEA-Pd NPs, OAm-Pd NPs, Bare-Pd NPs, OAm/C, DEA/C and C were evaluated, and products were quantified by using online GC for CO and H_2, and IC for $HCOO^-$ (Fig. S13 in Supporting information). All reported potentials are referred to the reversible hydrogen electrode (RHE) unless otherwise noted. The linear sweep voltammetry (LSV) curves (scan rate = 20 mV/s) were

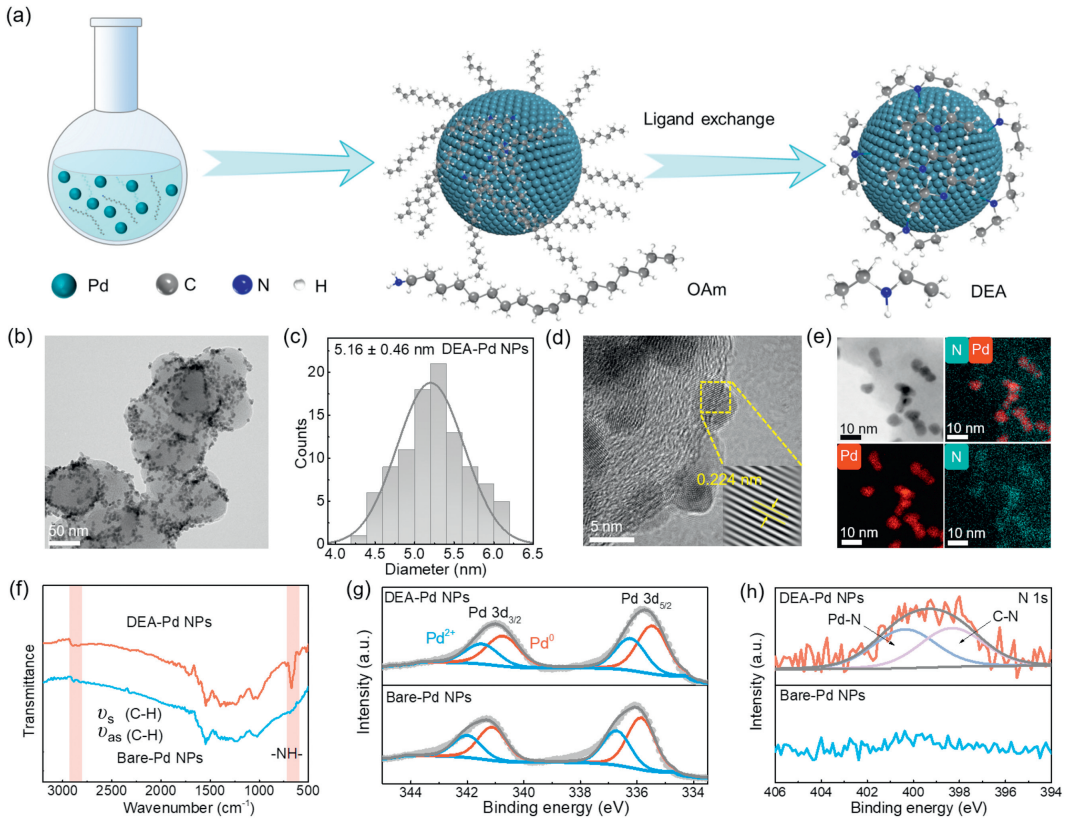


Fig. 2. (a) Scheme for synthesizing DEA-Pd NPs. (b) TEM image, (c) size statistics, (d) HRTEM image, and (e) EDS mappings of DEA-Pd NPs. (f) FTIR spectra, XPS spectra of (g) Pd 3d and (h) N 1s of Bare-Pd NPs and DEA-Pd NPs, respectively.

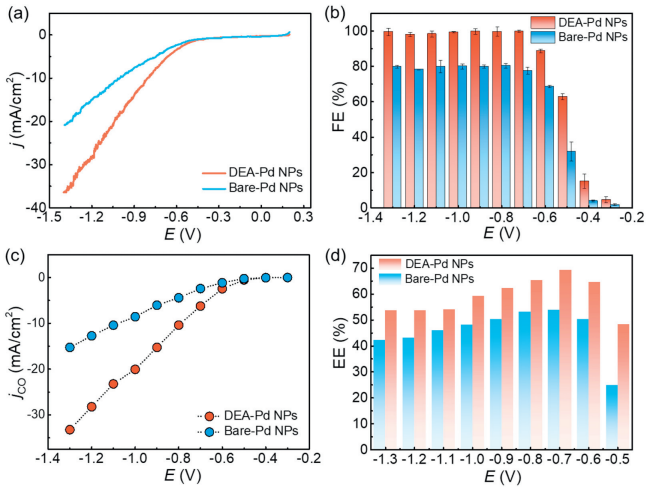


Fig. 3. (a) Cathodic LSV curves, (b) FE_{CO}, (c) j_{CO}, and (d) EEs of DEA-Pd NPs and Bare-Pd NPs.

depicted in Fig. 3a and Fig. S14 (Supporting information), which could roughly examine their potential electrocatalytic activity because *j* included the contribution from CO_2RR and HER. Clearly, DEA-Pd NPs showed an enhanced *j* of 36.5 mA/cm^2 at −1.4 V, whereas Bare-Pd NPs only reached 20.9 mA/cm^2. Following this, the potential-dependent product distribution on DEA-Pd NPs was carried out, and the results illustrated that DEA-Pd NPs exhibited an extremely high CO selectivity with a nearly 100% FE_{CO} over a wide potential window from −0.7 V to −1.3 V. Even at an ultralow potential of −0.6 V, DEA-Pd NPs still reached a FE_{CO} of around 90% (Fig. 3b), whereas OAm-Pd NPs and Bare-Pd NPs only achieved a FE_{CO} of 74.7% and 68.6%, respectively (Fig. S15 in Supporting information). In contrast with the Bare-Pd NPs, the amino ligand on OAm-Pd NPs also worked for CO_2RR. However, due to the steric effect, the long chain of OAm restricted the proximity of CO_2 to the surface-active site to some extent, which well explained the limited performance improvement of OAm-Pd NPs relative to DEA-Pd NPs. To confirm that the enhanced CO_2RR performance intrinsically originates from the chemically-bonded DEA on surface Pd atoms, *i.e.*, Pd–N bond, rather than the residual OAm or DEA adsorbed on carbon black, CO_2RR activity on OAm/C and DEA/C was further examined. As expected, the CO FE on DEA/C remained below 20% across the entire potential range, while OAm/C performed almost no CO_2RR activity. Importantly, the turnover frequency (TOF) results indicated that DEA-Pd NPs possessed a TOF value higher than DEA/C (Fig. S16 in Supporting information), and the same phenomenon also occurred on OAm-Pd NPs and OAm/C, implying that DEA and OAm could maximize the activity of Pd NPs only when chemically bonded with Pd NPs, and its promotion effect became more pronounced at more negative potentials. Besides, through integrating the *j* obtained at various potentials (Fig. S17 in Supporting information) and FE_{CO}, the CO partial *j* (j_{CO}) was plotted in Fig. 3c and Fig. S18 (Supporting information), which displayed the exact *j* contribution from CO_2RR. Clearly, the j_{CO} of DEA-Pd NPs was much higher than those of OAm-Pd NPs and Bare-Pd NPs, confirming its remarkable CO_2RR performance.

Although typical electrochemical indexes, such as *j* and FE, have confirmed the outstanding CO_2RR performance on DEA-Pd NPs, energy efficiency (EE) is currently receiving increasing attention as a leading indicator to assess its industrial feasibility and economic viability. Therefore, we calculated the EEs of CO_2RR and HER (Fig. S19 in Supporting information), respectively. It was found that

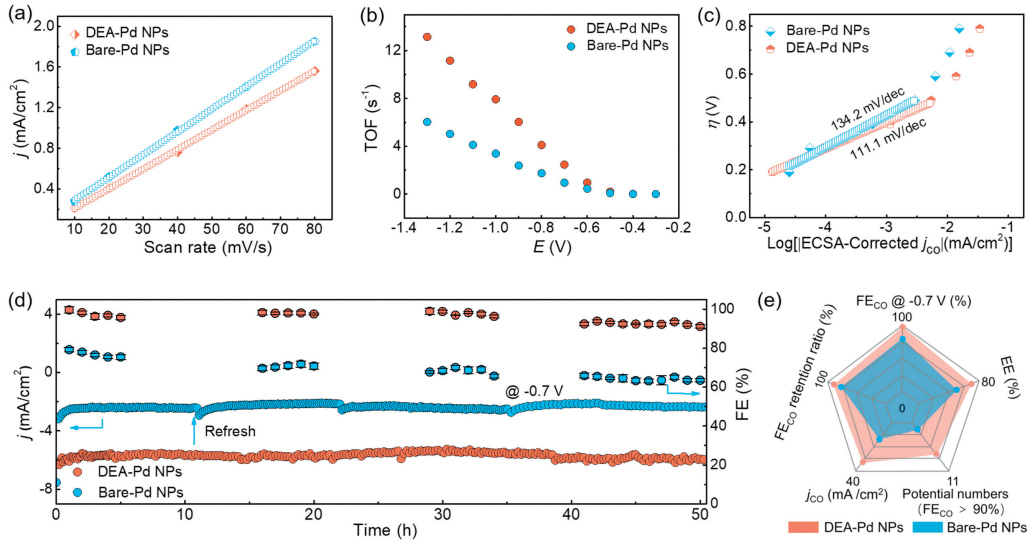


Fig. 4. (a) Plots of charging difference *versus* scan rate. (b) TOFs at different potentials. (c) Tafel plots. (d) Long-term stabilities of Bare-Pd NPs and DEA-Pd NPs, and (e) their radar map involving FE_{CO} retention ratio (*i.e.*, $FE_{CO(Final)}/FE_{CO(Initial)}$), FE_{CO} at −0.7 V, EE, j_{CO} and potential number (FE_{CO} > 90 %).

the EE toward CO_2RR on DEA-Pd NPs at −0.7 V was 69.2 %, much higher than that of Bare-Pd NPs (53.8 %), indicating that DEA-Pd NPs could reduce power input and production cost upon achieving the same output (Fig. 3d). Furthermore, the electrochemical double layer capacitance (C_{dl}) was measured to determine the electrochemical active surface areas (ECSAs) in pursuit of normalizing the activity and kinetics (Fig. 4a and Fig. S20 in Supporting information). Surprisingly, C_{dl} of DEA-Pd NPs was 19.32 mF/cm^2, relatively smaller than that of Bare-Pd NPs (22.36 mF/cm^2), probably due to the partial coverage of surface Pd atoms by DEA. However, the activity of a catalyst is normally governed by two principal factors, *i.e.*, the number and the intrinsic activity of active site. As expected, DEA-Pd NPs possessed a TOF value of 2.46 s^{-1} at −0.7 V, larger than Bare-Pd NPs (Fig. 4b), implying that the enhanced CO_2RR activity on DEA-Pd NPs was derived from the superior intrinsic activity of active sites induced by -NH- in DEA. This was further verified by the kinetics insights based on the ECSA-corrected Tafel plot of $\log[j_{(CO)}]$ *versus* η in Fig. 4c, where a Tafel slope of 111.1 mV/dec was achieved on DEA-Pd NPs, considerably smaller than that of 134.2 mV/dec on Bare-Pd NPs, which was also closer to the theoretical 118 mV/dec governed by the rate-determining step of $CO_2 + e^- \rightarrow CO_2^{\bullet-}$ [12,53]. In addition, during the stability test of 50 h at −0.7 V (Fig. 4d), DEA-Pd NPs maintained the FE_{CO} above 90 % and j at 5.8 mA/cm^2, whereas the FE_{CO} of Bare-Pd NPs decayed to 63 %, confirming the impressive stability of DEA-Pd NPs toward CO_2RR. To verify the structural stability of DEA-Pd NPs after long-term electrolysis, TEM image (Fig. S21 in Supporting information), EDX mappings (Fig. S22 in Supporting information), size distribution (Fig. S23 in Supporting information), FTIR tests (Fig. S24 in Supporting information) of DEA-Pd NPs were obtained. The results showed negligible changes in morphology, elemental distribution and particle size. Also, the characteristic absorption peaks of DEA were observed in DEA-Pd NPs, whereas they were not detected in $KHCO_3$ solution. These results confirmed that the excellent catalytic stability primarily originated from its robust structural stability. For a better holistic view, a radar map presenting stability reflected by FE_{CO} retention ratio, potential numbers with FE_{CO} over 90 %, FE, EE and j_{CO} was plotted in Fig. 4e. Apparently, all indicators of DEA-Pd NPs were far better than those of Bare-Pd NPs, highlighting the excellence of DEA in promoting CO_2RR. Furthermore, compared with other Pd-based catalysts (Table S1 in Supporting information), DEA-Pd NPs demonstrated a more outstanding CO_2RR performance, which further highlighted the crucial role of DEA in enhancing the CO_2RR performance of Pd NPs.

To uncover the underlying reaction pathway of DEA-Pd NPs toward CO_2RR, *in situ* FTIR measurements were conducted, and the results were shown in Figs. 5a and b, where the peaks at ~2106, ~1976 and ~1896 cm^{-1} were attributed to a CO linear configuration intermediate ($*CO_L$), a CO bridge adsorption configuration intermediate ($*CO_B$), and a triple-bound adsorption configuration intermediate ($*CO_T$), and, respectively [54]. Clearly, a transformation between $*CO_L$, $*CO_B$ and $*CO_T$ at different potentials was observed for both DEA-Pd NPs and Bare-Pd NPs. As the potential increased, the $*CO_L$ peak for Bare-Pd NPs became more prominent, while DEA-Pd NPs maintained a higher proportion of $*CO_L$ throughout the entire potential range, and the peak was gradually shifted to 2116 cm^{-1} due to the decrease in resonance frequency in the negative electric field caused by the Stark effect [55,56]. It was concluded that DEA on surface Pd atoms limited the formation of $*CO_B$ and $*CO_T$ adsorption configurations, but favored $*CO_L$ adsorption. This was because the increased hydrophobicity of DEA-Pd NPs influenced the local solvation environment, which could promote a more facile CO desorption, since the thinner water layer on the hydrophobic surface contributed to a better CO diffusion into the electrolyte, thereby leading to a higher proportion of $*CO_L$. Meanwhile, the presence of DEA could tune the electronic configuration of Pd, which weakened the surface adsorption of CO by providing more electrons to the Pd-CO antibonding orbital, which preferentially stabilized the $*CO_L$. Moreover, the $*CO_L$ only required a single Pd site, but the $*CO_B$ and $*CO_T$ involved multiple Pd atoms, which might be sterically hindered by the DEA on Pd surface, thus limiting the formation of $*CO_B$ and $*CO_T$ adsorption configurations and favoring the $*CO_L$ adsorption, thereby alleviating the CO poisoning on surface Pd atoms [57,58].

In addition, differential charge density was calculated, as shown in Fig. 5c and Fig. S25 (Supporting information), and the xyz table with coordinates of the optimized structures was demonstrated in Table S2 (Supporting information). Clearly, the charge density on DEA was depleted, whereas that at the interface of Pd and N was obviously accumulated. The Bader charge analysis indicated that Pd absorbed 0.21 e from DEA, suggesting that the N atom in DEA formed a strong Pd–N covalent bond with Pd, which donated electrons to Pd during CO_2RR. To further explore its elec-

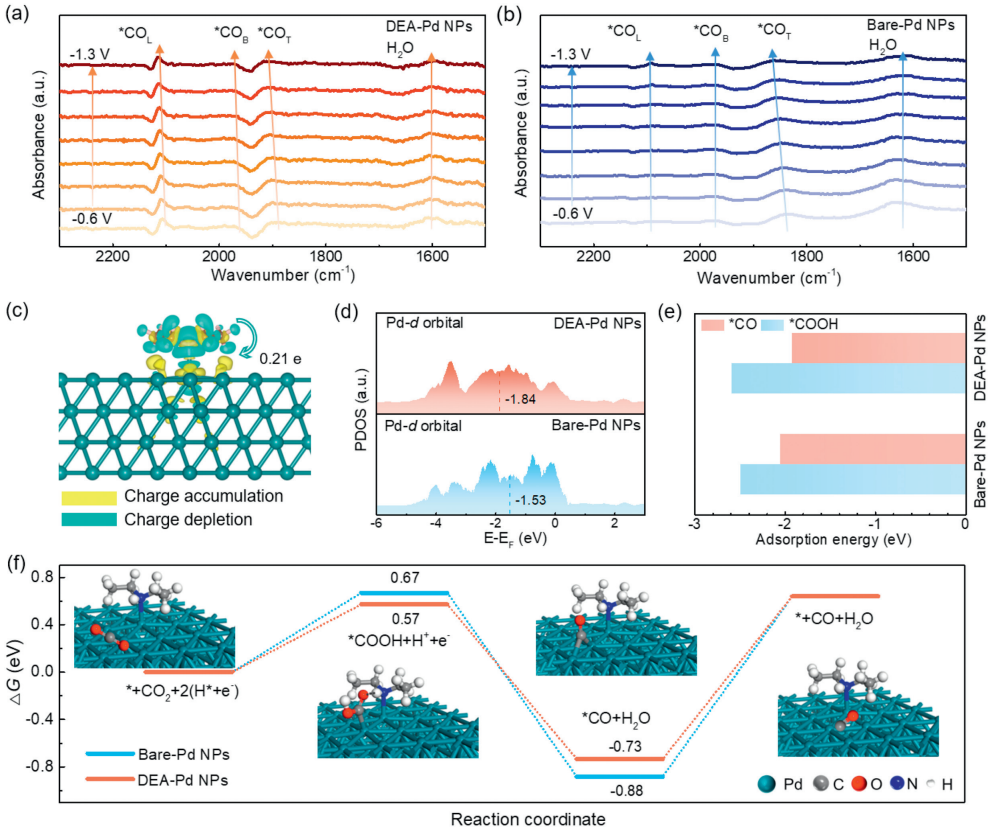


Fig. 5. Potential-dependent *in situ* FTIR patterns from −0.6 V to −1.3 V of (a) DEA-Pd NPs and (b) Bare-Pd NPs. (c) Differential charge density, (d) PDOS, (e) adsorption energy of *COOH and *CO, and (f) ΔG diagrams on DEA-Pd NPs and Bare-Pd NPs.

tronic structure, the partial density of states (PDOS) was calculated, and the results in Fig. 5d showed that the electrons of Bare-Pd NPs were squeezed due to the electron donation effect induced by DEA, resulting in the whole shift of Pd d-band center of DEA-Pd NPs from −1.53 eV to −1.84 eV. This was confirmed by previous studies that a lower Pd d-band center could weaken the surface adsorption of CO by providing more electrons to the Pd-CO antibonding orbital [15,59]. In addition, we compared the adsorption energies of key intermediates (*i.e.*, *CO, *COOH and *H) for DEA-Pd NPs and Bare-Pd NPs in Fig. 5e. It was found that the *COOH adsorption energy of −2.59 eV on DEA-Pd NPs was larger than that of −2.49 eV on Bare-Pd NPs, together with a lower *CO adsorption energy of −1.92 eV. This demonstrated that DEA-Pd NPs was beneficial to *COOH adsorption and *CO desorption, which precisely addressed the CO poisoning issue on Pd-based materials. With one step forward, the profiles of Gibbs free energy (*i.e.*, ΔG) diagrams for CO_2RR to CO over DEA-Pd NPs and Bare-Pd NPs were displayed in Fig. 5f. Apparently, DEA-Pd NPs experienced a lower energy barrier of only 0.57 eV for the first proton-coupled electron transfer step (*i.e.*, $CO_2 + H^+ + e^- \rightarrow$ *COOH) than Bare-Pd NPs (0.67 eV). Similarly, the energy required to proceed the CO desorption step (*i.e.* $*CO \rightarrow * + CO$) was 1.37 eV on DEA-Pd NPs, energetically more favorable than 1.52 eV on Bare-Pd NPs. All in all, the underlying mechanism was thus inferred that –NH– in the Pd–N bond formed H-bonds with *COOH in the first proton-coupled electron transfer step, which served as the driving force for DEA-Pd NPs to deliver a stronger *COOH adsorption ability. Meanwhile, the left shift of d-band center caused by the electron donating effect of DEA simultaneously inhibited the adsorption of *CO. It is thus concluded that through precisely tuning the electronic structure and distribution, the adsorption energy of *COOH and *CO could be individually tailored, indicating a deviation from the conventional linear scaling relationship, which typically assumed a synchronized increase or decrease in *COOH and *CO adsorption strength.

In summary, we developed a "one stone killing two birds" DEA-mediated strategy to functionalize surface Pd atoms by ligand exchanging the residual OAm on the ultrafine Pd NPs with DEA instead of deliberately removing it, and explored its crucial role toward CO_2RR. DFT calculations revealed that the electron donation effect of DEA could compress the electrons of Pd, which thus lowered the Pd d-band center, and weakened the CO surface adsorption by providing more electrons to the Pd-CO antibonding orbital. Moreover, the selective H-bond formation at the first proton-coupled electron transfer step accelerated the *COOH adsorption, and as such, the unfavorable linear scaling relationship of the isochronously increased or decreased adsorption energies of *COOH and *CO were broken. As a result, DEA-Pd NPs achieved a FE_{CO} close to 100% in an ultrawide potential window from −0.7 V to −1.3 V and a high CO selectivity exceeding 90% for over 50 h. Therefore, the smart reverse design will open up new possibilities to address the residual issue of ligands on different nanostructure during synthesis, and extend the ligand utilization toward various electrocatalytic systems.

Declaration of competing interest

The authors declare that they have no known competing financial interests or personal relationships that could have appeared to influence the work reported in this paper.

CRediT authorship contribution statement

Mulin Yu: Writing – original draft, Investigation, Formal analysis, Data curation, Conceptualization. **Shuo Liu:** Data curation.

Yufeng Tang: Methodology, Data curation. **Guoqiang Lu:** Data curation. **Linbo Liu:** Data curation. **Pengfei Sui:** Data curation. **Xianzhu Fu:** Data curation. **Subiao Liu:** Writing – review & editing, Visualization, Supervision, Project administration, Methodology, Funding acquisition, Conceptualization. **Yifei Sun:** Writing – review & editing, Supervision. **Jingli Luo:** Writing – review & editing, Supervision.

Acknowledgments

This work is supported by the Pilot Group Program of the Research Fund for International Senior Scientists (No. 22350710789) and the Start-up Funding of Central South University (No. 206030104). The authors are grateful for resources from the High-Performance Computing Center of Central South University.

Supplementary materials

Supplementary material associated with this article can be found, in the online version, at doi:10.1016/j.cclet.2025.111958.

References

[1] R. Li, C.W. Tung, B. Zhu, et al., J. Colloid Interface Sci. 674 (2024) 326–335.
[2] R. Li, F. Xie, P. Kuang, et al., Small 20 (2024) 2402867.
[3] Q. Cheng, M. Huang, Q. Ye, B. Deng, F. Dong, Chin. Chem. Lett. 35 (2024) 109112.
[4] D. Gao, H. Zhou, F. Cai, et al., ACS Catal. 8 (2018) 1510–1519.
[5] B. Jiang, X.G. Zhang, K. Jiang, D.Y. Wu, W.B. Cai, J. Am. Chem. Soc. 140 (2018) 2880–2889.
[6] S. Chatterjee, C. Griego, J.L. Hart, et al., ACS Catal. 9 (2019) 5290–5301.
[7] J.S. Diercks, J. Herranz, M. Georgi, et al., ACS Catal. 12 (2022) 10727–10741.
[8] J. Fan, H. Du, Y. Zhao, et al., ACS Catal. 10 (2020) 13560–13583.
[9] J.T. Ren, L. Chen, H.Y. Wang, Y. Feng, Z.Y. Yuan, Energy Environ. Sci. 17 (2024) 3960–4009.
[10] X. Tan, C. Yu, X. Song, et al., Nano Energy 104 (2022) 107957.
[11] D. Xiao, X. Bao, M. Zhang, et al., Chem. Eng. J. 452 (2023) 139358.
[12] S. Liu, H. Tao, L. Zeng, et al., J. Am. Chem. Soc. 139 (2017) 2160–2163.
[13] H. Zhang, C. He, S. Han, et al., Chin. Chem. Lett. 33 (2022) 3641–3649.
[14] H. Jia, Y. Yang, T.H. Chow, et al., Adv. Funct. Mater. 31 (2021) 2101255.
[15] Y. Zhou, R. Zhou, X. Zhu, et al., Adv. Mater. 32 (2020) 2000992.
[16] D. Wu, G. Huo, W. Chen, X.Z. Fu, J.L. Luo, Appl. Catal. B: Environ. 271 (2020) 118957.
[17] W. Xie, B. Li, L. Liu, et al., Chem. Soc. Rev. 54 (2025) 898–959.
[18] F. Ye, S. Zhang, Q. Cheng, et al., Nat. Commun. 14 (2023) 2040.
[19] M. Jiang, M. Zhu, M. Wang, et al., ACS Nano 17 (2023) 3209–3224.
[20] Y. Liu, Z. Jiang, C. Huang, et al., Nano Lett. 23 (2023) 5911–5918.
[21] X. Kong, J. Zhao, Z. Xu, et al., J. Am. Chem. Soc. 145 (2023) 14903–14911.
[22] M.N. Khrizanforov, F.F. Naileva, K.A. Ivshin, et al., Dalton Trans. 53 (2024) 17351–17360.
[23] J. Chen, G. Wang, Y. Dong, et al., Angew. Chem. Int. Ed. 64 (2025) e202416367.
[24] V.V. Khrizanforova, R.R. Fayzullin, S.V. Kartashov, et al., Chem. Eur. J. 30 (2024) e202400168.
[25] G. Yang, J. Huang, W. Gu, et al., Proc. Natl. Acad. Sci. U. S. A. 122 (2025) e2419434122.
[26] X. Chen, J. Chen, N.M. Alghoraibi, et al., Nat. Catal. 4 (2021) 20–27.
[27] A. Thevenon, A. Rosas-Hernández, J.C. Peters, T. Agapie, Angew. Chem. 131 (2019) 17108–17114.
[28] J. Tamura, A. Ono, Y. Sugano, C. Huang, et al., Phys. Chem. Chem. Phys. 17 (2015) 26072–26078.
[29] Q. Fan, K. Liu, Z. Liu, et al., Part. Part. Syst. Char. 34 (2017) 1700075.
[30] Z. Wang, Y. Zhou, C. Xia, et al., Angew. Chem. 133 (2021) 19255–19260.
[31] X.K. Qi, M.J. Zheng, C. Yang, et al., J. Am. Chem. Soc. 145 (2023) 16630–16641.
[32] Z. Liu, X. Lv, S. Kong, et al., Angew. Chem. Int. Ed. 62 (2023) e202309319.
[33] W. Chen, Y. Wang, F. Wang, et al., Adv. Mater. 36 (2024) 2411802.
[34] S. Choi, S. Parameswaran, J.-H. Choi, Phys. Chem. Chem. Phys. 23 (2021) 12976–12987.
[35] Q. Luo, H. Duan, M.C. McLaughlin, et al., Chem. Sci. 14 (2023) 9664–9677.
[36] S. Yoo, S. Yoo, G. Deng, et al., Adv. Mater. 36 (2024) 2313032.
[37] M. Dack, Chem. Soc. Rev. 4 (1975) 211–229.
[38] E. Breynaert, M. Houlleberghs, S. Radhakrishnan, et al., Chem. Soc. Rev. 49 (2020) 2557–2569.
[39] Y. Wang, Y. Liu, P. Cao, et al., ACS Appl. Mater. Interfaces 16 (2024) 20587–20596.
[40] M. Zhuansun, Y. Liu, R. Lu, et al., Angew. Chem. 135 (2023) e202309875.
[41] K. Chen, M. Cao, Y. Lin, et al., Adv. Funct. Mater. 32 (2022) 2111322.
[42] R. Li, H. Li, X. Zhang, et al., Adv. Funct. Mater. 34 (2024) 2402797.
[43] Z. Ouyang, G. Sheng, Y. Zhong, et al., Angew. Chem. Int. Ed. 64 (2025) e202418790.
[44] S. Chen, S. Li, R. You, et al., ACS Catal. 11 (2021) 5666–5677.
[45] J. Luo, Y. Zhou, S. Yang, et al., ACS Appl. Mater. Interfaces 15 (2023) 22025–22035.
[46] D. Hemmeter, U. Paap, N. Taccardi, et al., ChemPhysChem 24 (2023) e202200391.
[47] X. Xiao, S. Lin, L. Zhang, et al., Nano Res. 15 (2022) 2928–2934.
[48] J. Huang, M. Klahn, X. Tian, et al., Angew. Chem. 136 (2024) e202400174.
[49] J. Sun, H. Yang, W. Gao, T. Cao, G. Zhao, Angew. Chem. 134 (2022) e202211373.
[50] Q. Chen, X. Zhou, X. Zhang, et al., ACS Appl. Mater. Interfaces 14 (2022) 20988–20996.
[51] C. Feng, X. Ouyang, Y. Deng, J. Wang, L. Tang, J. Hazard. Mater. 441 (2023) 129845.
[52] H. Guo, J. Raj, Z. Wang, et al., Small 20 (2024) 2311132.
[53] J.F. Xie, J.J. Chen, Y.X. Huang, et al., Appl. Catal. B: Environ. 270 (2020) 118864.
[54] S. Wei, Y. Xu, T. Song, et al., J. Am. Chem. Soc. 147 (2025) 4219–4229.
[55] L. Zhang, X. Yang, Q. Yuan, et al., Nat. Commun. 14 (2023) 8311.
[56] C. Liu, M. Wang, J. Ye, et al., Nano Lett. 23 (2023) 1474–1480.
[57] Q. Liu, Q. Jiang, L. Li, W. Yang, J. Am. Chem. Soc. 146 (2024) 4242–4251.
[58] Z. Jin, M. Yang, Y. Dong, et al., Nano-Micro Lett. 16 (2024) 4.
[59] N. Zhang, X. Zhang, Y. Kang, et al., Angew. Chem. 133 (2021) 13500–13505.